npj computational materials

www.nature.com/npjcompumats

ARTICLE OPEN

Effect of spin-orbit coupling on the high harmonics from the topological Dirac semimetal Na_3Bi

Nicolas Tancogne-Dejean[1,2]✉, Florian G. Eich[3] and Angel Rubio[1,2,4,5]✉

In this work, we performed extensive first-principles simulations of high-harmonic generation in the topological Diract semimetal Na_3Bi using a first-principles time-dependent density functional theory framework, focusing on the effect of spin-orbit coupling (SOC) on the harmonic response. We also derived an analytical model describing the microscopic mechanism of strong-field dynamics in presence of spin-orbit coupling, starting from a locally $U(1) \times SU(2)$ gauge-invariant Hamiltonian. Our results reveal that SOC: (i) affects the strong-field excitation of carriers to the conduction bands by modifying the bandstructure of Na_3Bi, (ii) makes each spin channel reacts differently to the driven laser by modifying the electron velocity (iii) changes the emission timing of the emitted harmonics. Moreover, we show that the SOC affects the harmonic emission by directly coupling the charge current to the spin currents, paving the way to the high-harmonic spectroscopy of spin currents in solids.

npj Computational Materials (2022)8:145 ; https://doi.org/10.1038/s41524-022-00831-6

INTRODUCTION

The swift development of strong-field attoscience in solids has recently allowed for the development of many novel techniques, such as laser picoscopy of valence electrons[1] or attosecond metrology in solids[2], tailored toward controlling electron dynamics in solids on unprecedented timescales[3–5]. Among the possible applications of controlled strong-field dynamics in solids, one finds the possibility to perform high-harmonic spectroscopy of various fundamental phenomena on femto- to attosecond timescales, such as bandstructure dynamics[6–11], dynamical correlation effects[12–14], or the study of structural and topological phase transitions[15,16]. Given the wealth of physical phenomena occurring in solids, much more exciting results are expected to emerge in the coming years.

Recently, topological effects, and the related Berry curvature effects, have attracted a lot of attention in the context of strong-field dynamics[17–21]. In particular, several studies investigated how high-harmonic generation (HHG) is affected by a topological phase transition using the Haldane model[15,16,22] and related Haldane nanoribons models[23], and a more recent work investigated HHG in three-dimensional topological insulators[24]. In order to demonstrate the possibility to probe topological phase transitions using high-harmonic generation in a experiment, one needs to find a material that can host these different phases, and for which one can, by tuning an external parameter, reach different parts of its phase diagram. In this respect, Na_3Bi was shown to be a very promising material, as its phase diagram is extremely rich and displays different topologically non-trivial phases, such as topological Dirac and Weyl semimetal phases, topological and trivial insulating phases, or a phase with non-trivial Fermi surface states with non-zero topological charges[25]. Without breaking any system symmetry, Na_3Bi is a three-dimensional (3D) topological Dirac semimetal[26] where two overlapping Weyl fermions form a 3D Dirac point. It was shown that a compression of 1% along the y axis, which breaks inversion symmetry, can turn Na_3Bi into a topological insulator. Moreover, circularly-polarized light can be employed to break time-reversal symmetry. Ab initio calculations for Na_3Bi driven by such circularly-polarized light showed that it induces a Floquet-Weyl semimetal where the two Weyl points are separated in momentum space[27]. Importantly, because in this case the crystal symmetries of Na_3Bi are still preserved, these Weyl points remain topologically protected[25]. The capability to selectively break some of the symmetries of Na_3Bi either using pressure, or ultrafast circularly-polarized light pulses, allows to explore its phase diagram. However, before exploring the complex phase diagram of Na_3Bi, one needs to get a deeper understanding of the strong-field response in Na_3Bi in its pristine phase. This is the main scope of the present work.

At the hearth of many topological properties and Berry-curvature-related phenomena in quantum materials lies the spin-orbit coupling (SOC) interaction. While SOC does not affect strongly HHG in atomic systems, mostly affecting the harmonic yield[28], it is known that the SOC can strongly modify the bandstructure of bulk materials, and is responsible for various phenomena such as spin-Hall currents[29], the anomalous Hall effect[30], and spintronics[31], to cite a few. Understanding how the SOC affects the strong-field dynamics in solids is therefore of paramount importance in order to later understand related phenomena such as topology. This is also why Na_3Bi is a very attractive choice, as it allows us to investigate SOC effects, without any Berry-curvature-related phenomena.

It is clear that SOC can modify the bandstructure of materials, and can, for instance, lead to band-inversion and thus induce topological insulators. SOC can also split energy bands and lift spin degeneracy, and renormalize electronic bands. Besides these modifications of the bandstructure, one might wonder if or how the SOC affects the dynamics of the excited carriers within these modified bands. Already, in the absence of any external laser field, by considering the lowest relativistic correction to the Pauli Hamiltonian containing the spin-orbit interaction

[1]Max Planck Institute for the Structure and Dynamics of Matter and Center for Free-Electron Laser Science, Luruper Chaussee 149, 22761 Hamburg, Germany. [2]European Theoretical Spectroscopy Facility (ETSF), Donostia-San Sebastian, Spain. [3]HQS Quantum Simulations GmbH, Haid-und-Neu-Straße 7, D-76131 Karlsruhe, Germany. [4]Nano-Bio Spectroscopy Group, Universidad del País Vasco, 20018 San Sebastián, Spain. [5]Center for Computational Quantum Physics (CCQ), The Flatiron Institute, 162 Fifth Avenue, New York, NY 10010, USA. ✉email: nicolas.tancogne-dejean@mpsd.mpg.de; angel.rubio@mpsd.mpg.de

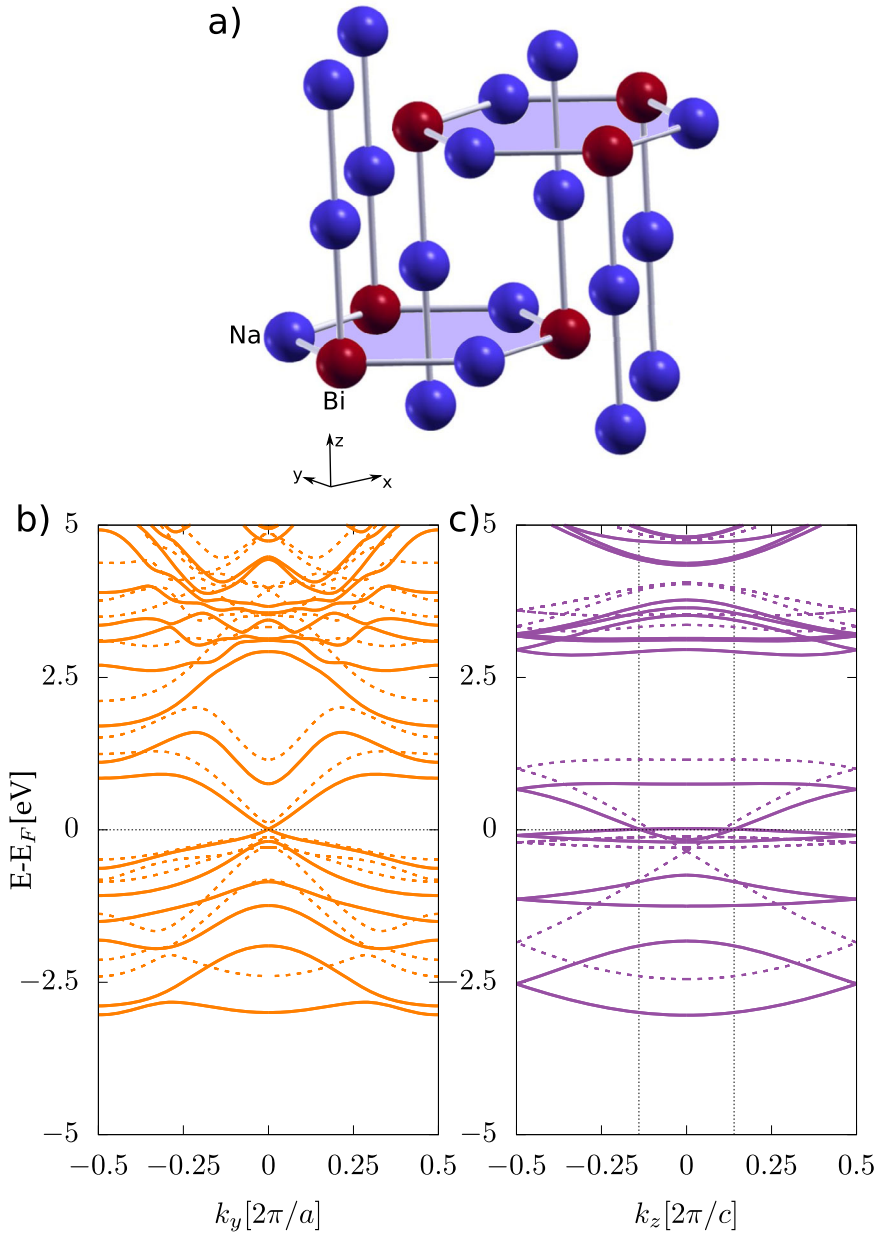

Fig. 1 Structural and electronic properties of Na_3Bi. a Structure of bulk Na_3Bi. **b** Band dispersion of Na_3Bi along the k_y direction, for $k_x = 0$ and $k_z = 0.28\,\pi/c$, where c is the out-of-plane lattice parameter. **c** Band dispersion of Na_3Bi along the k_z direction, for $k_x = k_y = 0$. The vertical lines indicate the position of the two Weyl points. The dashed lines represent the bandstructure without SOC.

$H_{SO} = \frac{he}{4m^2c^2}\mathbf{p}.(\boldsymbol{\sigma}\times\nabla V)$, where V is the potential due to the ions acting on the electrons and $\mathbf{p}$ their momentum, one finds that the velocity operator is modified such that $\hat{\mathbf{v}} = -\frac{i}{\hbar}[\hat{\mathbf{r}}, \hat{H}] = \frac{1}{m}[\mathbf{p} + \frac{e}{c}\mathcal{A}]$, where $\mathcal{A} = \frac{\hbar}{4mc}\boldsymbol{\sigma}\times\nabla V$ plays the role of a SU(2) gauge vector potential[32]. This can be seen as leading to an effective magnetic field $\mathcal{B} = \nabla\times\mathcal{A} = \hbar[\boldsymbol{\sigma}.(\nabla^2 V) - (\boldsymbol{\sigma}.\nabla)\nabla V]/(4mc)$. How the change of the electrons' velocity induced by the SOC reflects in the strong-field response of solids is one of the main focus of this work. As we will see later, this change in the electrons' velocity leads to a coupling between the charge current and the microscopic fluctuations of the spin current. Furthermore, because of minimal coupling, the spin-orbit interaction is itself modified by light. However, this effect is usually negligible, as discussed below.

The relation between spin-current and nonlinear response of bulk material has already been partly investigated in the context of perturbative nonlinear optics. It was shown that a pure spin-current can induce a nonlinear response in GaAs in the form of a non-zero perturbative second-harmonic generation along specific directions [33,34]. It is therefore interesting to ask if HHG in solids could be used to measure spin currents. In ref. [35], authors investigated theoretically the optical and spin harmonics emitted from iron monolayers, showing that the spin current displays a similar harmonic structure as the HHG obtained from the charge current. Whereas they showed that the spin current also exhibit non-perturbative harmonics that depends on the specific symmetries of their system, a discussion on how the HHG is directly influenced by the spin current remains elusive. To answer this question, we derived here the exact equation of motion of the physical charge current starting from a locally U(1) × SU(2) gauge invariant Hamiltonian,[36,37] including spin-orbit coupling.

The outline of this paper is as follows. In Results, we discuss some electronic properties of Na_3Bi, and we study its strong-field electron dynamics, focusing on the effect of spin-orbit coupling on its strong-field response. In Equation of motion of charge current,

we present the derivation of the equation of motion of the conserved charge current for a U(1) × SU(2) locally gauge-invariant Hamiltonian, including necessary relativistic corrections. In particular, we obtain, in the lowest order in $1/c$ a formula for HHG in presence of spin-orbit coupling for non-magnetic materials. Finally, we draw our conclusions in Discussion. The details of the ab initio method used to model the electron dynamics in Na_3Bi are given in Methods.

RESULTS

Using our ab initio TDDFT framework, we study HHG in bulk Dirac semimetals, taking Na_3Bi as a prototypical material. Its crystalline structure is shown in Fig. 1 a). A key feature to describe the electronic structure of Na_3Bi is the SOC. The effect of SOC on the bandstructure of Na_3Bi is also shown in Fig. 1. Without SOC, Na_3Bi is metallic, but does not display Dirac points at the Fermi energy, whereas SOC leads to the appearance of two Dirac cones at the Fermi energy, located at $(0, 0, \pm 0.28\,\pi/c)$, in good agreement with the measured position of the Dirac cones in pristine Na_3Bi[26].

The modifications of the bandstructure induced by the SOC should affect the strong-field dynamics. Indeed, the curvature of the bands is modified, which will modify any intraband motion and the corresponding harmonic emission mechanism. The energy separation between valence and conduction bands is modified, which will affect both the excitation of carriers to the conduction bands and the interband harmonic emission by recombination of electron-hole pairs. In the following, we will show that besides these expected changes, solely due to the change of the material's bandstructure, we observe clear effects due to the change of the electron's velocity due to the SU(2) gauge vector potential.

High-harmonic generation spectra

We start by analyzing the harmonic response of the Na_3Bi when excited by linearly-polarized and circularly-polarized laser fields. To be general, we consider here both $y-z$ and $x-y$ polarization planes, as shown in Fig. 2. Clear odd-structure harmonics are obtained in both cases, even if no clear plateau are observed in these spectra. Few points can be noticed directly: i) the intensity of the harmonics emitted from a circularly-polarized driver is not really much smaller than the one obtained for a linearly-polarized driver. In fact, for a laser polarized in the $x-y$ plane (Fig. 2b)) the harmonic emission is even stronger for the circularly-polarized driver. An intense harmonic response to circularly polarized light is interesting as it can be used to produce high-energy photons which are circularly polarized[38], but it also can lead to a non-perturbative circular photogalvanic effect in this material. Latter, we will exploit the similarity of the linearly and circularly polarized light to unveil the role of the SOC on the excitation of carriers to the conduction bands. ii) The highest observed harmonics seems to be the same in all the cases, except for the linearly polarized driver in the $x-y$ polarization plane. As a consequence, we will focus on the following on the $y-z$ polarization plane for which the harmonic emission is stronger. iii) the two polarization planes lead to qualitatively different results for circularly polarized drivers. Indeed for the $y-z$ plane, all odd harmonics are obtained for a circularly-polarized driver whereas for the $x-y$ case, we observe two consecutive odd harmonics over three, the last one been suppressed, which means we observe harmonics 5, 7 but not 9, and so on. While this result looks surprising at first glance, it is only the result of selection rules[39] for different symmetries of the different polarization planes, as already discussed and confirmed experimentally by some of us [11,38] and others[40]. Indeed, in the case of the $x-y$ polarization plane, the six-fold lattice symmetry leads to the suppression of the third harmonics, whereas the fifth and the seventh are not forbidden[39], as observed for instance in quartz[38]. In the case of the $y-z$ polarization, the four-fold symmetry leads to odd harmonics with alternating ellipticity, as observed in silicon or bulk MgO[11,38].

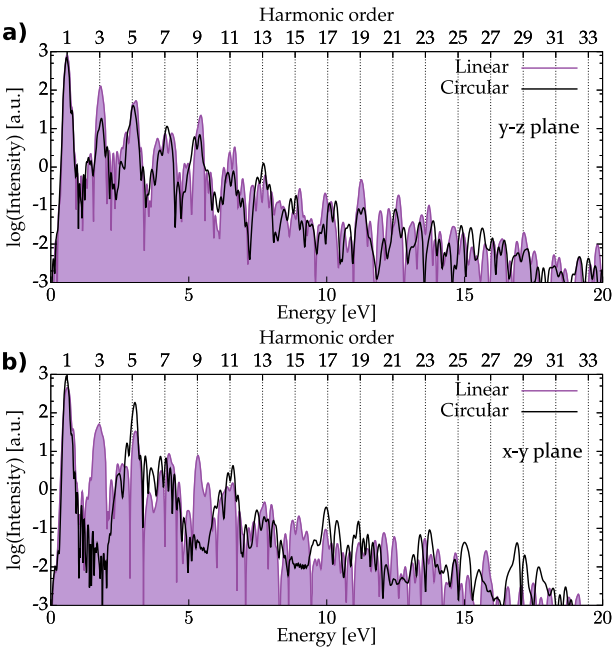

Fig. 2 High-harmonic generation from Na_3Bi. Harmonic spectra obtained for linearly-polarized driving field (violet curves) and for circularly-polarized driving field (black lines) for (**a**) the $y-z$ polarization plane, and (**b**) the $x-y$ polarization plane.

Electron dynamics and SOC

We now turn our attention to the number of electron excited by the laser pulse. In a carrier excitation process, the bandgap plays a key role in the excitation, and the excitation rate rate depends exponentially on it. We therefore expect that the number of excited electrons strongly depends on the details of the solid bandstructure in the case of interband excitation (Zener tunneling). In order to reveal the role of SOC on the excitation of carriers to conduction bands, we computed the number of excited carriers in Na_3Bi for a linearly-polarized laser, as well as a left-hand-side (LHS) circularly polarized laser field, as shown in Fig. 3 for the same intensity. This plot shows clearly that more electrons are excited to the conduction bands when the SOC is included, irrespective of what is the polarization state of the light (see bottom panel). In the linearly polarized case, we observe clear virtual excitations at twice the frequency of the laser field, whereas in the circularly-polarized case, these oscillations are not present. This can be understood as follows: in the circularly-polarized case, electrons are ionized twice more often than in the linearly polarized case during the laser pulse, every time each components of the field reaches an extrema. Moreover, because the field strength along each direction is reduced by a factor $1/\sqrt{2}$ for a circularly-polarized laser compared to the linearly-polarized case, excitation is roughly reduced by the same amount. This reduction of ionization for lower field strength is what we expect from single-photon excitation through interband excitation. After the end of the pulse, the two pulses have still excited similar amount of electrons. However, the contribution from the SOC (see Fig. 3c) does not show a dependence on the polarization state nor the strength of the driver during the laser pulse, as it is almost identical for both linearly and circularly-polarized laser pulses, whose field strength differ by a factor $1/\sqrt{2}$. We interpret the fact that the carrier excitation induced by SOC does not depend on the field strength as originating not from interband transitions, but

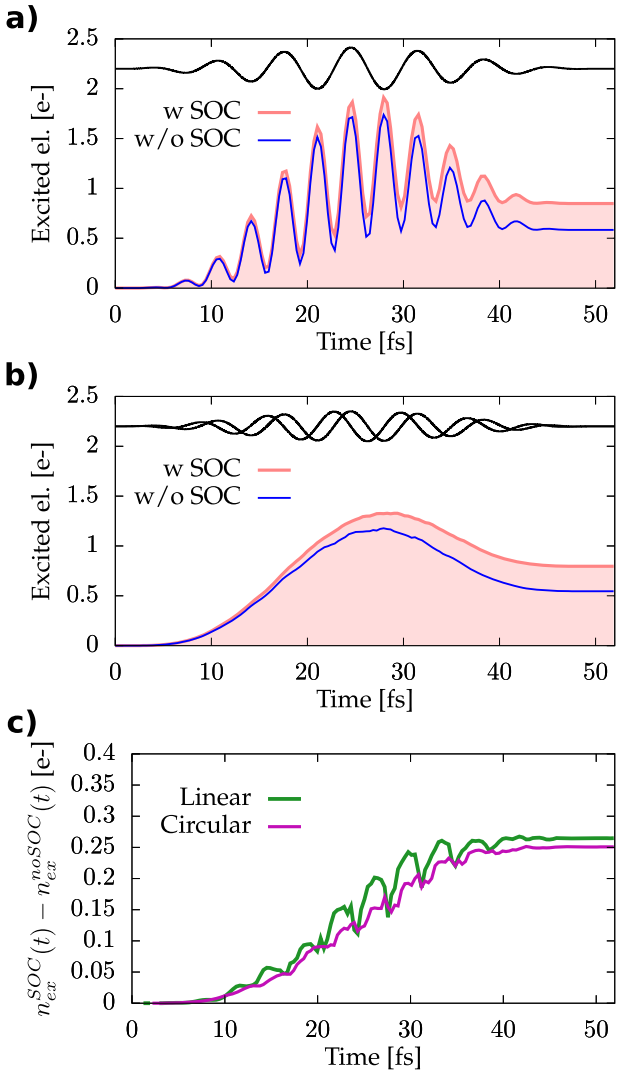

Fig. 3 Effect of SOC on the number of excited carriers. Number of excited electrons for (**a**) a linearly-polarized laser field along the y axis, and (**b**) a LHS circularly-polarized laser pulse with a major axis along the y axis (middle panel), for an intensity in matter of $I_0 = 4\times10^{11}$ W.cm^{-2}. In each panel, the blue curve corresponds to the result without SOC and the shaded area corresponds to the result including SOC. **c** Shows the difference in the number of excited electrons induced by SOC, for the linearly polarized and for the circularly polarized cases. In (**a**) and (**b**), the time evolution of the vector potential is shown in black.

from an intraband acceleration of carriers, through the Dirac points that appear when SOC is included. Finally, we note that the number of electrons is obtained here by a projection on the field-free states, which yield a gauge-dependent number of electrons during the laser pulse. However, we are interested here not in the quantitative values during the laser field, but by how this quantity depends on the polarization state of the driver. Moreover at the end of the laser pulse the results are again gauge invariant, which makes our above analysis robust.

Effect of SOC on the charge and spin currents

Spin-orbit coupling is a key physical ingredient needed to properly describe the topological nature of Na_3Bi. It is therefore interesting to investigate how much the strong-field electron dynamics is affected by the presence of SOC. As discussed in the introduction, the spin-orbit coupling introduces a spin-dependent gauge vector

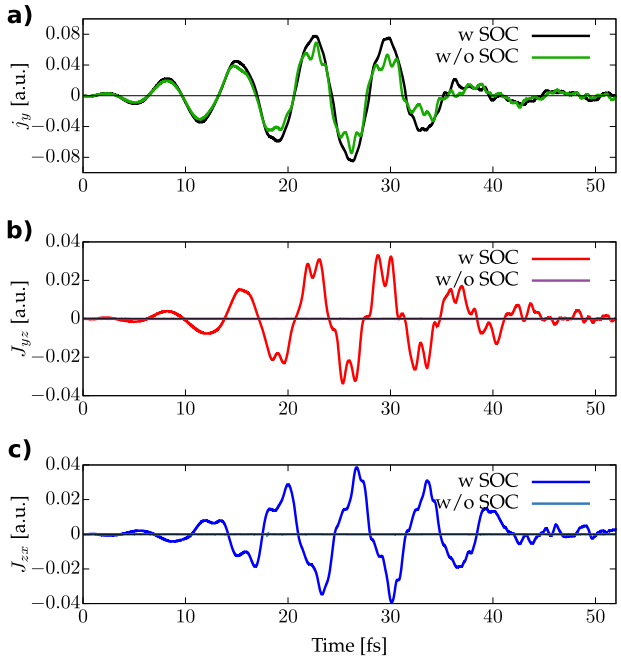

Fig. 4 Effect of SOC on the charge and spin currents. a Calculated charge current along the y axis, for a RHS circularly-polarized driver in the $y-z$ plane with and without SOC. **b**, **c** Show respectively the J_{yz} and J_{zx} components of the corresponding spin current. See the main text for more details.

field $\mathcal{A} = \frac{\hbar}{4mc}\boldsymbol{\sigma}\times\nabla V$. This term leads to a different velocity of the electrons, depending on their spin, which directly implies that alongside with a charge current, there will be spin currents generated by the intense driving field when SOC is included.

We therefore computed both the charge current and the spin-current induced by the laser field, defined in second quantization as

$$\hat{J}_{ij}(\mathbf{x}) = -\frac{i\hbar}{2m}\left[\hat{\psi}^\dagger(\mathbf{x})\hat{\sigma}_i(\nabla_j\hat{\psi}(\mathbf{x})) - (\nabla_j\hat{\psi}(\mathbf{x}))^\dagger\hat{\sigma}_i\hat{\psi}(\mathbf{x})\right], \quad (1)$$

where $\hat{\sigma}_i$ are the Pauli matrices. Similar to Eq. (9), there is a contribution from the nonlocal operators that is omitted here for conciseness.

In absence of SOC, no spin currents are induced in the material, as Na_3Bi is non-magnetic. This is clearly shown in Fig. 4 where we show the calculated charge current (panel a)) alongside with some components of the spin current (panels b)-c)). Including the SOC, the electrons will behave differently depending on their spin, because of the presence of the spin-dependent gauge vector potential that modifies their velocity. Now we address the importance of these spin currents, compared to the magnitude of the charge current, especially for a nonmagnetic material like Na_3Bi. We found that the non-zero components of the macroscopic spin currents (J_{xx}, J_{zx}, J_{yy}, and J_{yz} for a laser circularly polarized in the $y-z$ plane, J_{zx}, J_{zy}, J_{xz}, J_{yz} for a laser circularly polarized in the $x-y$ plane) all have very similar magnitude, and we found that this magnitude is only half of the magnitude of the charge current, as shown in Fig. 4 for the case of a circularly-polarized driver. Our simulations thus reveal that strong driving fields can generate very efficiently spin currents, even when the electrons with different spin "feel" the same bandstructure. This shows that the modification of the electron's velocity due to the SOC is not negligible. The spin currents, similar to the charge current, exhibit fast oscillations. We found (not shown here) that the harmonic spectra of the different components of the spin currents display an odd-harmonic structure, and exhibit the same energy cutoff as the charge current, in agreement with the results

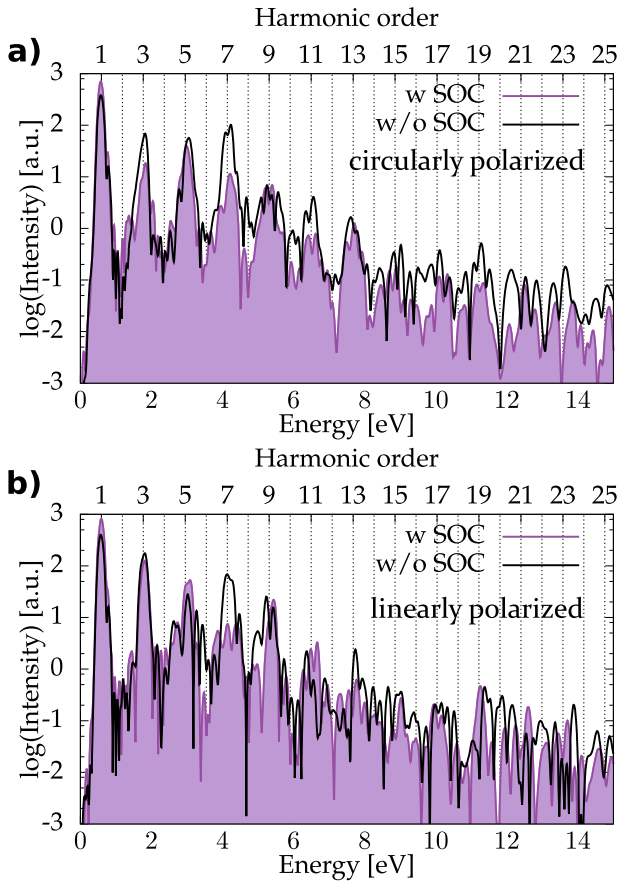

Fig. 5 Effect of SOC on the HHG spectra. Calculated HHG spectra with (violet curves) and without SOC (black curves) for (**a**) a laser RHS circularly polarized in the $y-z$ plane, and (**b**) a laser linearly polarized along the y axis. Similar to the other simulations, we employ here a laser pulse of 25 fs duration, a carrier wavelength λ of 2100 nm, and an intensity of $I = 4\times10^{11}$ W.cm^{-2}.

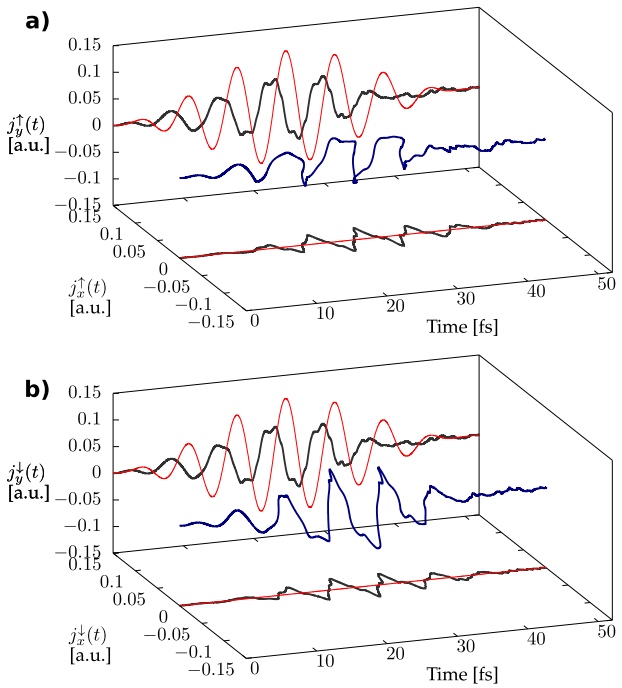

Fig. 6 Spin-resolved electron dynamics in presence of SOC. Calculated electronic current (blue) for the (**a**) up spin channel, and (**b**) down spin channel for a linearly-polarized laser field along the y axis. The projections of the current on the x and y axis are shown in black. The time profile of the vector potential is shown in red.

of ref. [41] for Rashba and Dresselhaus models of SOC. The direct connection between spin currents and charge current, and thus HHG, is derived analytically and discussed in Equation of motion of charge current. Therefore, we focus in the following of this section on the effect of the SOC on harmonic response of the charge current.

As shown in Fig. 4a), the SOC also modifies the dynamics of the charge current. The charge current obtained in presence of SOC (black curve) is smoother than without SOC (green curve), and resembles more the time profile of the exciting laser pulse. This indicates that high-frequency components are reduced in the time-dependent current, i.e., weaker harmonics are present in its power spectrum. We can directly see that the SOC reduces the harmonic response of the material by looking at the HHG spectra, see Fig. 5. For both linear and circularly polarized laser pulses, we obtain that SOC increases the linear response of the material while decreasing the yield of the harmonics. This result is counter-intuitive, as we showed before that the SOC leads to more electrons excited in the conduction bands. It thus appears that more excited carriers do not directly reflect into more intense harmonic emission, which implies the carrier dynamics in presence of SOC, including their trajectories and recombination, is modified. We cannot simply understand the effect of SOC on the basis of a modified band structure, but we need to take into account how SOC reshape the electrons' dynamics within these bands.

To further understand how the SOC can lead to less harmonic emission while more carriers are emitted, we analyzed the individual contribution of each spin channel to the charge current ($\mathbf{j}(\mathbf{r},t) = \mathbf{j}^{\uparrow\uparrow}(\mathbf{r},t) + \mathbf{j}^{\downarrow\downarrow}(\mathbf{r},t)$). As shown in Fig. 6, the spin-dependent effective magnetic field induced by the SOC leads to a transverse motion of each individual spins, thus leading to an elliptically polarized emission from the individual spin channels, even for a linearly-polarized electric field. Again, we obtain that the spin-dependent gauge vector field has a important effect on the electron^'s velocity. As the effective magnetic field flips sign for each spin channel, the current associated with each of the two spin channels are of opposite ellipticity. However, because spins are degenerate in Na_3Bi, the transverse currents associated with each spin channel cancel each other, and no net transverse current is obtained, as shown in Fig. 6 for a linearly polarized driving field. This cancellation of the individual contributions of the transverse current leads to a smaller magnitude for the total electronic current, which reflects directly as a lower harmonic yield.

The component of the spin-resolved current along the direction of the laser is also modified, as shown in Fig. 4. However, this change cannot be easily distinguished from the change in the electronic band curvature, also induced by the SOC. Still, the modification of electrons' velocity leads to modified motion of the carriers in the bands, and we therefore expect a time-delay in the harmonic emission compared to the case in absence of SOC, due to the transverse motion of the carriers. We have performed a time-frequency analysis of the harmonic emission with and without SOC, as shown in Fig. 7, to analyze if the timing of the harmonic emission is modified in presence of SOC, as we expect from the result of Fig. 6. From the result of our time-frequency analysis, we found that the main emission event occurs at a later time when SOC is included (with a time delay of roughly 500 attoseconds), as expected from the motion of electron in presence of an effective magnetic field. The side structures are also shifted in a similar way. We also note a slightly more pronounce chirp of

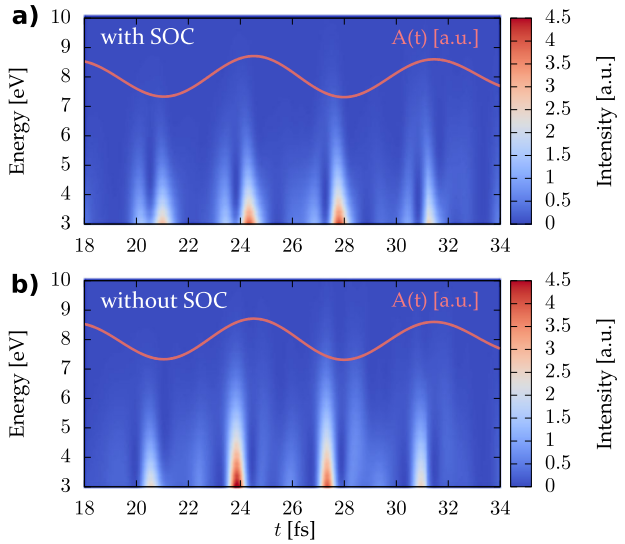

Fig. 7 Effect of SOC on the timing of the harmonic emission. Time-frequency analysis of the harmonic emission driven by a linearly-polarized laser field, (**a**) with SOC, and (**b**) without SOC. The width of the Gabor transform is taken as a third of the period of the laser pulse, corresponding to a time of 0.37 fs. The time profile of the driving laser field is also shown as a solid line.

the emission in presence of the SOC. Finally, we found (not shown here) that a similar time delay occurs for circularly polarized laser fields, confirming that the modification of the temporal shape of the harmonic emission is present irrespective of the polarization state of the driving pulse. Overall, the modifications of the time of harmonic emission in presence of SOC demonstrate that the SOC modifies significantly the velocity of the carriers, and affects their motion in the bands. This clearly demonstrate that the modifications of the bandstructure alone account for all the changes in the HHG induce by SOC.

EQUATION OF MOTION OF THE CHARGE CURRENT

The equation of motion of the charge current, in absence of SOC, has been shown to provide valuable insights, for instance in the context of HHG in solids[10]. Therefore, in this section, we aim at deriving the equation of motion for the physical charge current, in presence of spin-orbit coupling.

We first consider the single-particle Pauli Hamiltonian describing a particle of mass m and charge e in an external electromagnetic field,

$$\hat{h}(t) = \frac{1}{2m}\hat{\mathbf{\Pi}}^2(t) - eV(t) + \frac{eh}{2mc}\mathbf{B}(t).\hat{\boldsymbol{\sigma}} + \frac{eh}{8m^2c^2}\left[\hat{\mathbf{\Pi}}(t).(\hat{\boldsymbol{\sigma}}\times\mathbf{E}(t)) + (\hat{\boldsymbol{\sigma}}\times\mathbf{E}(t)).\hat{\mathbf{\Pi}}(t)\right], \tag{2}$$

where the canonical momentum is given by $\hat{\mathbf{\Pi}}(t) = \frac{\hbar}{i}\nabla + \frac{e}{c}\mathbf{A}(t)$, the magnetic field $\mathbf{B}(t)$ is given by $\mathbf{B}(t) = \nabla\times\mathbf{A}(t)$, where $\mathbf{A}(t)$ is the vector potential of the external field, and the electric field is given by $\mathbf{E}(t) = -\nabla V(t) - \frac{1}{c}\partial_t\mathbf{A}(t)$, with V the external scalar potential acting on the electrons. The first two terms describe respectively the kinetic energy and the potential energy of the particle. The third one is the Zeeman term, and the last one corresponds to the spin-orbit coupling term. Importantly, the SOC contained in Eq. (2) allow for describing the part of the spin-orbit coupling induced by the light, which is responsible for important physical effects, such as the inverse Faraday effect[42].

While the previous Hamiltonian has been considered in many theoretical work, it is possible to obtain a local $U(1)\times SU(2)$ symmetry by including a term of the higher order $O(1/m^3)$ as explained in ref. [36]. The motivation for this choice lies in the fact that this will allow us later to define a $U(1)\times SU(2)$ gauge-invariant spin-current, which we defined in this work as the physical spin current, see Supplementary Information.

From this Hamiltonian, the equation of motion of the physical charge current is obtained, see the Supplementary Information. It is clear that this equation of motion contains many different contributions, which are not easy to analyze. In fact, it is easier to analyze the equation of motion of the macroscopic charge current, which is the source term of Maxwell equation, and therefore represent the emitted electric field. In a periodic system, the interaction term, as well as the divergences vanish, and therefore we obtain for the macroscopic average of the physical charge current, denoted $\left\langle\hat{\mathbf{j}}_{\mathrm{phys},k}(t)\right\rangle$,

$$\begin{aligned}\frac{\partial}{\partial t}\left\langle\hat{\mathbf{j}}_{\mathrm{phys},k}(t)\right\rangle = \int_\Omega d\mathbf{x}\Big(&-\frac{e}{m}\left[\hat{n}\mathbf{E} + \frac{1}{c}\hat{\mathbf{j}}_{phys}\times\mathbf{B}\right]_k + \frac{eh}{4m^2c^2}\left[\hat{\mathbf{m}}\times\partial_t\mathbf{E}\right]_k \\ &- \frac{e^2h}{4m^3c^3}\left[(\hat{\mathbf{m}}\times\mathbf{B})\times\mathbf{E}\right]_k - \frac{eh}{2m^2c}\sum_p \hat{m}_p\left(\partial_k(B_p)\right) \\ &+ \frac{eh}{4m^2c^2}\sum_{pqr}\hat{J}_{phys,pq}\left(\epsilon_{kpr}\partial_q E_r - \epsilon_{qpr}\partial_k E_r + \frac{e}{2mc^2}\epsilon_{kqr}E_p E_r\right)\Big).\end{aligned} \tag{3}$$

Equation (3) is nothing but a force-balance equation, and the right-hand-side terms are the external forces acting of the electrons. We directly identify the first term as the Lorentz force. In absence of spin-orbit coupling, this is the only force term present in the equation of motion of the macroscopic charge current. The third term appears only when an electric field and a magnetic field coexist (see ref. [32] and references therein). The fourth term is a spin force that appears in presence of a non-uniform magnetic field, and was first evidenced by the Stern and Gerlach experiment. We note that the second term, which relates the magnetization of the electron to the external electric field, is also related to non-uniform magnetic field, if we assume that the external fields fulfill Maxwell equations. Finally, we also get a spin transverse force given by the term $\left[\mathbf{E}\circ\left\langle\hat{\mathbf{J}}_{phys}\right\rangle\right]\times\mathbf{E}$ (here "$\circ$" means a dot product on the spin index), which was discussed in ref. [32]. This force is proportional to the square of the electric field, and the spin current whose polarization is projected along the electric field. It is the counterpart of the force acting on a charged particle in a magnetic field $\mathbf{j}\times\mathbf{B}$, in which the spin current replaces the charge current, and the electric field replaces the magnetic field

In order to proceed with the analysis of the equation of motion, we split the electric-field $\mathbf{E}$ into a contribution from the electron-ion potential v_{ext}, which we assume to be time independent (ions are clamped), and a part originating from the laser field $\mathbf{E}_l$, assumed to be uniform (dipole approximation). Moreover, we assume that no external magnetic field is present. This leads to three contributions:

i) a part coming from the laser field

$$\frac{\partial}{\partial t}\left\langle\hat{\mathbf{j}}_{\mathrm{laser}}(t)\right\rangle = -\frac{e}{m}N_e\mathbf{E}_l + \frac{eh}{4m^2c^2}\langle\hat{\mathbf{m}}\rangle\times\partial_t\mathbf{E}_l + \frac{e^2h}{8m^3c^4}\left[\mathbf{E}_l\circ\left\langle\hat{\mathbf{J}}_{phys}\right\rangle\right]\times\mathbf{E}_l, \tag{4}$$

ii) an external part, from the electron-ion potential

$$\begin{aligned}\frac{\partial}{\partial t}\left\langle\hat{j}_{\mathrm{ext},k}(t)\right\rangle = -\int_\Omega d\mathbf{x}\Big(&\frac{e}{m}\hat{n}[\nabla v_{\mathrm{ext}}]_k \\ &- \frac{eh}{4m^2c^2}\sum_{pqs}\hat{J}_{phys,pq}\left[(\epsilon_{kps}\partial_q\partial_s v_{\mathrm{ext}}) - (\epsilon_{qps}\partial_k\partial_s v_{\mathrm{ext}})\right. \\ &\left.+ \frac{e}{2mc^2}\epsilon_{kps}(\partial_q v_{\mathrm{ext}})(\partial_s v_{\mathrm{ext}})\right]\Big),\end{aligned} \tag{5}$$

and iii) a part containing cross terms coupling the electron-ion potential to the laser field

$$\frac{\partial}{\partial t}\left\langle\hat{\mathbf{j}}_{\mathrm{cross}}(t)\right\rangle = \frac{e^2\hbar}{8m^3c^4}\int_\Omega d\mathbf{x}\left(\left[\mathbf{E}_l\circ\hat{\mathbf{J}}_{phys}\right]\times(\nabla v_{\mathrm{ext}}) + \left[(\nabla v_{\mathrm{ext}})\circ\hat{\mathbf{J}}_{phys}\right]\times\mathbf{E}_l\right). \tag{6}$$

Let us analyze the terms we are getting. The first term in Eq. (4) of the laser contribution is the remaining of the Lorentz force. It is present

without spin-orbit coupling but is not responsible for any harmonic, as it only contains the frequency components of the external laser field. The second term in Eq. (4) is related to the macroscopic magnetization of the system. In a non-magnetic material, such as Na_3Bi, this term vanishes. Finally, we get in Eq. (4) an high-order term coming from the spin transverse force. We implemented this term, as it is not taken care by the pseudopotentials as this is the case for the usual SOC, and checked that it is indeed numerically negligible. The cross terms in Eq. (6) contain high-order contributions ($O(1/c^4)$), and are therefore negligible here. Finally, we turn our attention to the external contributions, given by Eq. (5). As a first term, we obtain the part coming from the Lorentz force, plus a high-order derivative of the electron-ion potential, that can be interpreted as a mass renormalization term. Given that this is also a high-order term, we also neglect it. In fact, among all the SOC-related terms, only the second part of Eq. (5) contains a term that does not scale as $1/c^4$ but as $1/c^2$ for non-magnetic materials. We therefore expect that the term scaling as $1/c^2$ will be the dominant contribution when SOC is included.

Retaining only this term, we obtain to the lowest order in $1/c$ and for a non-magnetic materials such as Na_3Bi, a modified expression for HHG in presence of SOC only expressed in terms of gauge-invariant quantities

$$\mathrm{HHG}(\omega) \propto \sum_k \Big| \mathrm{FT}\Big\{ \int_\Omega d^3\mathbf{r} n(\mathbf{r},t)\partial_k v_{\mathrm{ext}}(\mathbf{r}) + \frac{\hbar}{4mc^2}\sum_{pqs}\hat{J}_{phys,pq}(\mathbf{r},t)\left[\epsilon_{kps}\partial_q\partial_s v_{\mathrm{ext}}(\mathbf{r}) - \epsilon_{qps}\partial_k\partial_s v_{\mathrm{ext}}(\mathbf{r})\right]\Big\} + N_e\mathbf{E}(\omega)\Big|^2. \quad (7)$$

Equation (7) is the main result of this section. It provides important physical insights into the effect of the spin-orbit coupling on HHG in non-magnetic materials. Indeed, this shows that the spin current is a source term for the equation of motion of the charge current, and therefore directly imprints into the emitted harmonic light. More precisely, we note that only the microscopic fluctuations of the spin current contribute to this extra term, and hence the HHG cannot be directly used as a probe of macroscopic spin currents. This formula offers an alternative perspective to the effect of the SOC on the strong-field response of bulk materials. The SOC does not simply modify the HHG by affecting the bandstructure of the materials, it also couples the charge current dynamics to the one of the spin current. This is the direct consequence of the change in velocity of the electrons, induced by the effective SU(2) gauge vector potential. Finally, let us comment on the fact that we considered here a non-magnetic material. If the material is magnetic, our equation of motion Eq. (3) contains another contribution to the lowest order in the relativistic corrections, which deserves to be investigated, in particular in presence of demagnetization. Some of the higher-order contributions are also leading to harmonic emission along different directions, where there should not be any emission if SOC is omitted; and terms containing an electric field will lead to even-order harmonic emission. Therefore one might be able to measure these terms independently of the rest of the systems' response. A similar idea was already used to measure an effective Berry curvature in quartz from the measured HHG spectra[43], and our equation of motion offers many directions to use a similar logic to probe microscopic details of spin and charge current. We plan to investigate the precise role of these different terms in future works.

DISCUSSION

In conclusion, we investigated the effect of the SOC on the strong-field electron dynamics in the topological Dirac semimetal Na_3Bi. We showed that the SOC affects the strong-field response by modifying the electronic band-structure of the material, which controls the injection of carriers to the conduction bands. Beside, we showed that the SOC modifies the velocity of the electrons in the bands by acting as a spin-dependent effective magnetic field. As a consequence, the spin-resolved electronic current becomes elliptically polarized, even for a linearly-polarized pump laser field. This modified trajectories modify the motion of the carriers, and lead to a time delay in the harmonic emission. We then derived the equation of motion of the total charge current from a locally gauge-invariant $U(1)\times SU(2)$ Hamiltonian properly describing the spin-orbit coupling in presence of a light field. From this, we showed that the SOC couples the charge current to the spin current, and we derived a formula for the HHG including to the lowest order relativistic corrections. This relation between charge and spin currents opens interesting perspectives for the optical spectroscopy of spin currents. Moreover, our equation of motion Eq. (3) can be applied to other materials, such as magnetic materials, for which other relativistic corrections might play a dominant role.

Finally, let us make some connection to some recent results obtained for the topological phase transition in the Haldane model. The increase of the number of excited electrons, as well as a time delay in the emission time of the harmonics has been identified as signatures of non-trivial topological phase[16], and the origin of these changes was associated to the Berry curvature of the material. Our results show that similar effects are obtained if we just include SOC, in a material which has no Berry curvature. The reason is that the Berry curvature can be seen as an effective magnetic field in momentum space[44], which also affects carriers trajectories[45]. How electrons evolve in materials having both SOC and Berry curvature (topological ground state), and which effect dominates will of course require more detailed analysis, and should be the subject of future works.

METHODS

Calculations were performed in the framework of real-time time-dependent density-functional theory (TDDFT), which has been shown to yield valuable information both the microscopic[10,12,38,46] as well as macroscopic [47,48] mechanisms leading to the HHG in solids and low-dimensional materials[49–51]. In this work, we use an in-plane lattice parameter of $a = 5.448$ Å and an out-of-plane lattice parameter $c = 9.655$ Å taking as the structure the one of ref. [25], a real-space spacing of $\Delta r = 0.36$ Bohr, and a $28\times28\times15$ **k**-point grid to sample the Brillouin zone. We employ norm-conserving fully relativistic Hartwigsen-Goedecker-Hutter (HGH) pseudopotentials, and we included spin-orbit coupling unless stated differently. Because we are interested in shedding light on the role of SOC on the microscopic response to strong fields, we are not considering macroscopic effects like propagation effects due to the coupling with Maxwell equations in the present calculations. These propagation effects are important for thick samples (as shown in ref. [47]), but are expected to only play a minor role in thin samples and in reflection geometry. Moreover, in all the calculations, the ions are kept fixed and the coupled electron-ion dynamics is not considered in what follows. This is justified as the fastest optical phonon in Na_3Bi has a periodic of 166 fs[52], which is much longer that the duration of our laser pulse. For such few-cycle driver pulses, the HHG spectra from solids have been shown to be quite insensitive to the carrier-envelope phase (CEP), which is therefore taken to be zero here. We consider a laser pulse of 25 fs duration (FWHM), with a sin-square envelope for the vector potential. The carrier wavelength λ is 2100 nm, corresponding to a carrier photon energy of 0.59 eV and the intensity of the laser field is taken to be $I = 4\times10^{11}$ W.cm^{-2} in matter. The time-dependent wavefunctions and current are computed by propagating Kohn-Sham equations within TDDFT, as provided by the Octopus package.[53] The time-dependent Kohn-Sham equation within the adiabatic approximation reads

$$i\hbar\frac{\partial}{\partial t}\left|\psi_{n,\mathbf{k}}(t)\right\rangle = \left[\frac{(\hat{\mathbf{p}}+e\mathbf{A}(t)/c)}{2m} + \hat{v}_{\mathrm{ext}} + \hat{v}_{\mathrm{H}}[n(\mathbf{r},t)] + \hat{v}_{\mathrm{xc}}[n(\mathbf{r},t)] + \hat{v}_{\mathrm{NL}}\right]\left|\psi_{n,\mathbf{k}}(t)\right\rangle, \quad (8)$$

where $|\psi_{n,\mathbf{k}}\rangle$ is a Pauli spinor representing the Bloch state with band index n, at the point **k** in the Brillouin zone, $\hat{v}_{\mathrm{ext}}$ is the electron-ion potential, $\mathbf{A}(t)$ is the external vector potential describing the laser field, $\hat{v}_{\mathrm{H}}$ is the Hartree potential, $\hat{v}_{\mathrm{xc}}$ is the exchange-correlation potential, and $\hat{v}_{\mathrm{NL}}$ is the non-local pseudopotential, also describing the spin-orbit coupling as commonly

done. As usual, the nonlocal pseudopotential contribution is made U(1) gauge invariant by properly including vector-potential phases[54]. However, as we will show later, this term is not enough to describe the U(1) × SU(2) gauge-invariant spin-orbit coupling. This is why we also included in $\hat{v}_{\mathrm{NL}}$ the term corresponding to the light-induced modification of the spin-orbit coupling, as derived and discussed in Equation of motion of charge current. In all our calculations, we employed the adiabatic local density approximation functional for describing the exchange-correlation potential. From the time-evolved wavefunctions, we computed the total electronic current $\mathbf{j}(\mathbf{r}, t)$,

$$\begin{aligned}\mathbf{j}(\mathbf{r},t) = &\tfrac{1}{2m}\sum_n \Re\big[\psi_n^*(\mathbf{r},t)(\hat{\mathbf{p}} + e\mathbf{A}(t)/c)\psi_n(\mathbf{r},t)\\ &- i\int d\mathbf{r}'\psi_n^*(\mathbf{r},t)[\hat{v}_{\mathrm{NL}},\hat{\mathbf{r}}]\psi_n(\mathbf{r}',t)\big],\end{aligned} \tag{9}$$

where the nonlocality of the pseudopotential contributes to the charge current and leads to a spin-orbit coupling contribution to it. From the knowledge of the total electronic current, the HHG spectrum is directly obtained as

$$\mathrm{HHG}(\omega) = \left|\mathrm{FT}\left(\frac{\partial}{\partial t}\int d\mathbf{r}\mathbf{j}(\mathbf{r},t)\right)\right|^2, \tag{10}$$

where FT denotes the Fourier transform.

The total number of electron excited to the conduction bands ($n_{\mathrm{ex}}(t)$) can be obtained by projecting the time-evolved wavefunctions ($|\psi_n(t)\rangle$) on the basis of the ground-state wavefunctions ($|\psi_{n'}^{\mathrm{GS}}\rangle$)

$$n_{\mathrm{ex}}(t) = N_e - \frac{1}{N_{\mathbf{k}}}\sum_{n,n'}^{\mathrm{occ.}}\sum_{\mathbf{k}}^{\mathrm{BZ}}\left|\left\langle\psi_{n,\mathbf{k}}(t)|\psi_{n',\mathbf{k}}^{\mathrm{GS}}\right\rangle\right|^2, \tag{11}$$

where N_e is the total number of electrons in the system, and $N_{\mathbf{k}}$ is the total number of **k**-points used to sample the BZ. The sum over the band indices n and n' run over all occupied states.

DATA AVAILABILITY

The data that support the findings of this study are available from the corresponding authors upon request, and will be deposited on the NoMaD repository.

CODE AVAILABILITY

The OCTOPUS code is available from http://www.octopus-code.org.

Received: 6 April 2021; Accepted: 16 June 2022;
Published online: 06 July 2022

REFERENCES

1. Lakhotia, H. et al. Laser picoscopy of valence electrons in solids. *Nature* **583**, 55–59 (2020).
2. Sommer, A. et al. Attosecond nonlinear polarization and light–matter energy transfer in solids. *Nature* **534**, 86–90 (2016).
3. Ghimire, S. & Reis, D. A. High-harmonic generation from solids. *Nat. Phys.* **15**, 10–16 (2019).
4. Kruchinin, S. Y., Krausz, F. & Yakovlev, V. S. Colloquium: Strong-field phenomena in periodic systems. *Rev. Mod. Phys.* **90**, 021002 (2018).
5. Li, J. et al. Attosecond science based on high harmonic generation from gases and solids. *Nat. Commun.* **11**, 1–13 (2020).
6. Vampa, G. et al. All-optical reconstruction of crystal band structure. *Phys. Rev. Lett.* **115**, 193603 (2015).
7. Lanin, A. A., Stepanov, E. A., Fedotov, A. B. & Zheltikov, A. M. Mapping the electron band structure by intraband high-harmonic generation in solids. *Optica* **4**, 516–519 (2017).
8. Li, L. et al. Determination of electron band structure using temporal interferometry. *Phys. Rev. Lett.* **124**, 157403 (2020).
9. Borsch, M. et al. Super-resolution lightwave tomography of electronic bands in quantum materials. *Science* **370**, 1204–1207 (2020).
10. Tancogne-Dejean, N., Mücke, O. D., Kärtner, F. X. & Rubio, A. Impact of the electronic band structure in high-harmonic generation spectra of solids. *Phys. Rev. Lett.* **118**, 087403 (2017).
11. Tancogne-Dejean, N., Mücke, O. D., Kärtner, F. X. & Rubio, A. Ellipticity dependence of high-harmonic generation in solids originating from coupled intraband and interband dynamics. *Nat. Commun.* **8**, 1–10 (2017).
12. Tancogne-Dejean, N., Sentef, M. A. & Rubio, A. Ultrafast modification of hubbard *u* in a strongly correlated material: Ab initio high-harmonic generation in nio. *Phys. Rev. Lett.* **121**, 097402 (2018).
13. Silva, R., Blinov, I. V., Rubtsov, A. N., Smirnova, O. & Ivanov, M. High-harmonic spectroscopy of ultrafast many-body dynamics in strongly correlated systems. *Nat. Phot.* **12**, 266–270 (2018).
14. Imai, S., Ono, A. & Ishihara, S. High harmonic generation in a correlated electron system. *Phys. Rev. Lett.* **124**, 157404 (2020).
15. Chacón, A. et al. Circular dichroism in higher-order harmonic generation: Heralding topological phases and transitions in chern insulators. *Phys. Rev. B.* **102**, 134115 (2020).
16. Silva, R., Jiménez-Galán, Á., Amorim, B., Smirnova, O. & Ivanov, M. Topological strong-field physics on sub-laser-cycle timescale. *Nat. Phot.* **13**, 849–854 (2019).
17. Jia, L., Zhang, Z., Yang, D. Z., Si, M. S. & Zhang, G. P. Probing magnetic configuration-mediated topological phases via high harmonic generation in $mnbi_2te_4$. *Phys. Rev. B* **102**, 174314 (2020).
18. Jiménez-Galán, Á., Silva, R., Smirnova, O. & Ivanov, M. Lightwave control of topological properties in 2d materials for sub-cycle and non-resonant valley manipulation. *Nat. Phot.* **14**, 728–732 (2020).
19. Bauer, D. & Hansen, K. K. High-harmonic generation in solids with and without topological edge states. *Phys. Rev. Lett.* **120**, 177401 (2018).
20. Jia, L. et al. High harmonic generation in magnetically-doped topological insulators. *Phys. Rev. B.* **100**, 125144 (2019).
21. Bai, Y. et al. High-harmonic generation from topological surface states. *Nat. Phys.* **17**, 311–315 (2021).
22. Moos, D., Jürß, C. & Bauer, D. Intense-laser-driven electron dynamics and high-order harmonic generation in solids including topological effects. *Phys. Rev. A* **102**, 053112 (2020).
23. Jürß, C. & Bauer, D. Helicity flip of high-order harmonic photons in haldane nanoribbons. *Phys. Rev. A* **102**, 043105 (2020).
24. Baykusheva, D. et al. Strong-field physics in three-dimensional topological insulators. *Phys. Rev. A* **103**, 023101 (2021).
25. Wang, Z. et al. Dirac semimetal and topological phase transitions in A_3bi (a = Na, k, rb). *Phys. Rev. B* **85**, 195320 (2012).
26. Liu, Z. et al. Discovery of a three-dimensional topological dirac semimetal, na3bi. *Science* **343**, 864–867 (2014).
27. Hübener, H., Sentef, M. A., De Giovannini, U., Kemper, A. F. & Rubio, A. Creating stable floquet–weyl semimetals by laser-driving of 3d dirac materials. *Nat. Commun.* **8**, 1–8 (2017).
28. Pabst, S. & Santra, R. Spin–orbit effects in atomic high-harmonic generation. *J. Phys. B: Atomic, Mol. Optical Phys.* **47**, 124026 (2014).
29. Sinova, J., Valenzuela, S. O., Wunderlich, J., Back, C. H. & Jungwirth, T. Spin hall effects. *Rev. Mod. Phys.* **87**, 1213–1260 (2015).
30. Nagaosa, N., Sinova, J., Onoda, S., MacDonald, A. H. & Ong, N. P. Anomalous hall effect. *Rev. Mod. Phys.* **82**, 1539–1592 (2010).
31. Žutić, I., Fabian, J. & Das Sarma, S. Spintronics: Fundamentals and applications. *Rev. Mod. Phys.* **76**, 323–410 (2004).
32. Shen, S.-Q. Spin transverse force on spin current in an electric field. *Phys. Rev. Lett.* **95**, 187203 (2005).
33. Wang, J., Zhu, B.-F. & Liu, R.-B. Second-order nonlinear optical effects of spin currents. *Phys. Rev. Lett.* **104**, 256601 (2010).
34. Werake, L. K. & Zhao, H. Observation of second-harmonic generation induced by pure spin currents. *Nat. Phys.* **6**, 875–878 (2010).
35. Zhang, G., Si, M., Murakami, M., Bai, Y. & George, T. F. Generating high-order optical and spin harmonics from ferromagnetic monolayers. *Nat. Commun.* **9**, 1–7 (2018).
36. Fröhlich, J. & Studer, U. M. Gauge invariance and current algebra in nonrelativistic many-body theory. *Rev. Mod. Phys.* **65**, 733–802 (1993).
37. Pittalis, S., Vignale, G. & Eich, F. G. U(1) × SU(2) gauge invariance made simple for density functional approximations. *Phys. Rev. B* **96**, 035141 (2017).
38. Klemke, N. et al. Polarization-state-resolved high-harmonic spectroscopy of solids. *Nat. Commun.* **10**, 1–7 (2019).
39. Tang, C. L. & Rabin, H. Selection rules for circularly polarized waves in nonlinear optics. *Phys. Rev. B* **3**, 4025–4034 (1971).
40. Saito, N. et al. Observation of selection rules for circularly polarized fields in high-harmonic generation from a crystalline solid. *Optica* **4**, 1333–1336 (2017).
41. Lysne, M., Murakami, Y., Schüler, M. & Werner, P. High-harmonic generation in spin-orbit coupled systems. *Phys. Rev. B* **102**, 081121 (2020).
42. Mondal, R. et al. Relativistic interaction hamiltonian coupling the angular momentum of light and the electron spin. *Phys. Rev. B* **92**, 100402 (2015).
43. Luu, T. T. & Wörner, H. J. Measurement of the berry curvature of solids using high-harmonic spectroscopy. *Nat. Commun.* **9**, 1–6 (2018).
44. Price, H. M., Ozawa, T. & Carusotto, I. Quantum mechanics with a momentum-space artificial magnetic field. *Phys. Rev. Lett.* **113**, 190403 (2014).

45. Xiao, D., Chang, M.-C. & Niu, Q. Berry phase effects on electronic properties. *Rev. Mod. Phys.* **82**, 1959–2007 (2010).
46. Otobe, T. High-harmonic generation in *α*-quartz by electron-hole recombination. *Phys. Rev. B* **94**, 235152 (2016).
47. Floss, I. et al. Ab initio multiscale simulation of high-order harmonic generation in solids. *Phys. Rev. A* **97**, 011401 (2018).
48. Yamada, S. & Yabana, K. Determining the optimum thickness for high harmonic generation from nanoscale thin films: An ab initio computational study. *Phys. Rev. B* **103**, 155426 (2021).
49. Tancogne-Dejean, N. & Rubio, A. Atomic-like high-harmonic generation from two-dimensional materials. *Science advances* **4**, eaao5207 (2018).
50. Le Breton, G., Rubio, A. & Tancogne-Dejean, N. High-harmonic generation from few-layer hexagonal boron nitride: Evolution from monolayer to bulk response. *Phys. Rev. B* **98**, 165308 (2018).
51. Mrudul, M., Tancogne-Dejean, N., Rubio, A. & Dixit, G. High-harmonic generation from spin-polarised defects in solids. *npj Computational Materials* **6**, 1–9 (2020).
52. Dong, X.-X., Chen, J.-X., Wang, Y., Lv, Z.-L. & Wang, H.-Y. Electronic, elastic and lattice dynamic properties of the topological dirac semimetal na3bi. *Materials Research Express* **6**, 076308 (2019).
53. Tancogne-Dejean, N. et al. Octopus, a computational framework for exploring light-driven phenomena and quantum dynamics in extended and finite systems. *The Journal of Chemical Physics* **152**, 124119 (2020).
54. Bertsch, G. F., Iwata, J.-I., Rubio, A. & Yabana, K. Real-space, real-time method for the dielectric function. *Phys. Rev. B* **62**, 7998–8002 (2000).

ACKNOWLEDGEMENTS

This work was supported by the European Research Council (ERC-2015-AdG694097), the Cluster of Excellence 'Advanced Imaging of Matter' (AIM), Grupos Consolidados (IT1249-19) and SFB925. The Flatiron Institute is a division of the Simons Foundation.

AUTHOR CONTRIBUTIONS

N.T.-D. performed all the calculations and code implementation. N.T.-D. and F.G.E. developed the theoretical model. All authors discussed the results and contributed to the final paper.

FUNDING

Open Access funding enabled and organized by Projekt DEAL.

COMPETING INTERESTS

The authors declare no competing interests.

ADDITIONAL INFORMATION

Supplementary information The online version contains supplementary material available at https://doi.org/10.1038/s41524-022-00831-6.

Correspondence and requests for materials should be addressed to Nicolas Tancogne-Dejean or Angel Rubio.

Reprints and permission information is available at http://www.nature.com/reprints

Publisher's note Springer Nature remains neutral with regard to jurisdictional claims in published maps and institutional affiliations.